Research Article Vol. 30, No. 6 / 14 Mar 2022 / Optics Express 8436
Optics EXPRESS

Imaging 3D molecular orientation by orthogonal-pair polarization IR microscopy

SHUYU XU,[1] JEREMY ROWLETTE,[2] AND YOUNG JONG LEE[1,*]

[1]*Biosystems and Biomaterials Division, National Institute of Standards and Technology, Gaithersburg, MD, USA*
[2]*DRS Daylight Solutions, San Diego, CA 92127, USA*
[*]*youngjong.lee@nist.gov*

Abstract: Anisotropic molecular alignment occurs ubiquitously and often heterogeneously in three dimensions (3D). However, conventional imaging approaches based on polarization can map only molecular orientation projected onto the 2D polarization plane. Here, an algorithm converts conventional polarization-controlled infrared (IR) hyperspectral data into images of the 3D angles of molecular orientations. The polarization-analysis algorithm processes a pair of orthogonal IR transition-dipole modes concurrently; in contrast, conventional approaches consider individual IR modes separately. The orthogonal-pair polarization IR (OPPIR) method, introduced theoretically but never demonstrated experimentally, was used to map the 3D orientation angles and the order parameter of the local orientational distribution of polymer chains in a poly(ε-caprolactone) film. The OPPIR results show that polymer chains in the semicrystalline film are aligned azimuthally perpendicular to the radial direction of a spherulite and axially tilted from the film normal direction. This newly available information on the local alignments in continuously distributed molecules helps to understand the molecular-level structure of highly anisotropic and spatially heterogeneous materials.

1. Introduction

Optical imaging of three-dimensional (3D) molecular distributions has been significantly advanced in sensitivity and resolving power. In contrast, imaging of optical anisotropy and molecular orientation remains in the 2D-projected directional maps, although molecular alignment occurs in 3D in natural and synthesized materials and affects their macroscopic physical, chemical, and biological properties [1–4]. Conventional 2D imaging approaches are based on polarization-controlled optical signals, such as birefringence [5,6], fluorescence [7,8], second harmonic generation [9,10], Raman scattering [11–14], and infrared (IR) absorption [15–19]. For example, polarization IR absorption microscopy has been widely used as a label-free chemical imaging tool for orientational information of specific IR modes of intrinsic molecules in various soft materials, such as biological tissues [15,20] and polymer films [17–19]. However, polarization IR microscopy, like other polarization-controlled imaging methods, can only measure the 2D projection of molecular orientation onto the polarization plane, and therefore, it cannot determine the out-of-plane angle of molecules. Even combining the 2D projected polarization profiles of multiple IR modes, the 3D orientational structures of ordered molecules or polymer chains can be constructed by comparing the experimental results with simulated polarization profiles [18,19], not by directly determining 3D angles. Due to the inability to measure the out-of-plane angle, the 2D-projected orientation measurement can characterize the orientational distribution function properly only when the sample symmetry axis can be assumed to lie in the polarization plane, such as fibers [21] and highly-stretched films [22].

Alternatively, by rotating the sample or the detector, X-ray scattering [23,24] and electron diffraction [25,26] can measure the 3D directions of atomic orientation, but these methods require precise control of sample and detector alignment and are often not suitable for imaging large-area organic samples with low scattering cross sections and fragility to the electron beam. IR-based optical spectroscopy of tilted samples has been used to measure the out-of-plane angles of

#449667 https://doi.org/10.1364/OE.449667

Received 3 Dec 2021; revised 28 Jan 2022; accepted 14 Feb 2022; published 28 Feb 2022

Optics EXPRESS

molecular orientation [27–30], but tilting the sample makes it difficult to use the approach for high-resolution optical imaging. Recently, researchers have developed new high-resolution imaging methods to measure the 3D orientation angles of highly dispersed objects by analyzing finely z-scanned defocused images [31,32], comparing with point spread functions [33], or detecting emissions from 2D-degenerate fluorophores [34,35]. However, those exquisite methods can be applied only to single molecules and crystals and isolated defects; thus, they are inappropriate for continuously distributed materials like polymers or tissues.

We recently proposed a simple algorithm that determines the 3D orientation angles from the 2D-projected polarization profiles of two non-parallel vibrational modes observed in the form of coherent Raman scattering [36] and IR absorption [37]. The new algorithm analyzes polarization anisotropies of the pair of vibrational modes concurrently, in contrast to conventional approaches of analyzing polarization-dependent signals from each aligned source separately. Thus, vibrational spectroscopy, such as IR and Raman, is more suitable for this approach than other unimodal optical signals because polyatomic molecules consisting of more than two atoms always have multiple non-parallel vibrational modes. An advantage of this analysis method for IR imaging is that it uses the 2D-projected polarization anisotropies observable with conventional polarization IR microscopy without requiring sample tilting or detector rotation. Another advantage is that the calculation is insensitive to sample thickness, density, and IR absorption cross section because it is based on polarization anisotropies, which is the ratio of the maximum and minimum absorption. Here, we present the first experimental results of 3D orientation angle images calculated by the concurrent analysis of an orthogonal-pair of polarization IR (OPPIR) data of a semicrystalline polymer film. The images of the 3D orientation angles and the local order parameter reveal the unique chain orientations in highly heterogeneous poly(ε-caprolactone) spherulites. In addition, potential sources of the uncertainty and the limitation of this new analysis method are discussed.

2. Experimental section

2.1. Sample

A poly(ε-caprolactone) (PCL, $M_n = 70\,000$–$90\,000$, Aldrich) in chloroform solution (3 mass%) was spin-cast onto a cover glass at 2000rpm for 30 s. After the film was dried in the air at room temperature overnight, it was melted at 70 °C and cooled to room temperature for re-crystallization. The annealing process was repeated three times, after which intact patterned PCL spherulites were observed by an optical microscope. The PCL thin film was then transferred to an IR transparent CaF_2 window. The thickness of the single PCL film was (5.5 ± 0.5) μm thick, measured three times at slightly shifted locations at the same sample by an ellipsometer. A scanning electron microscope (SEM) image of the spherulites in the film is presented in Supplement 1 Fig. S1.

2.2. Measurements

Polarization-controlled hyperspectral IR images of the PCL film were acquired with a wide-field QCL-IR microscope (Spero, Daylight Solutions, Inc., San Diego USA) with a compound refractive objective lens having a 0.7 numerical aperture (NA). Its simplified scheme can be found in Supplement 1 Fig. S2. The field of view was 650 μm × 650 μm, the pixel size was 1.4 μm, and the spatial resolution was approximately 5 μm. An achromatic IR half-wave plate (XCN, Gooch & Housego, retardation ≈ 180° ± 3° for 5 μm – 9 μm) was mounted to a computer-controlled rotation stage and embedded between the laser and the sample within the microscope. The performance of the achromatic IR half-wave plate was tested separately, yielding the extinction ratio of higher than 90 for all wavelengths (See Supplement 1 Fig. S3). The polarization extinction ratio of the entire microscopy system was measured by inserting a testing polarizer at the sample location.

Optics EXPRESS

The resulting extinction ratio was higher than 30 for 1000 cm^{-1}–1550 cm^{-1} (See Supplement 1 Fig. S4). This corresponds to less than 3% change in polarization anisotropy; thus, we did not consider a separate correction of the extinction ratio as a function of wavelength. An IR image was collected in transmission mode at each frequency while scanning the frequency from 1000 cm^{-1} to 1794 cm^{-1} with a 2 cm^{-1} increment. At a single location, 24 hyperspectral images were acquired as the achromatic waveplate was rotated with an 8° increment in polarization angle, η. The z-position of the objective lens was adjusted for each wavelength to compensate for chromatic aberration according to interpolated positions from previously measured focus positions. For the background reference measurement, the stage was translated to image a blank area of a pristine portion of the CaF_2 substrate at each polarization angle. At a fixed location, the total acquisition time for wide-field images over 398 frequency steps for 24 polarization steps was 44 min. The whole beam path from the laser to the detector inside the microscope enclosure was purged with dry nitrogen during data acquisition. The polarization angle of the incident light was calibrated by measuring the transmission through a polarizer located in place of the sample.

2.3. Data processing

Each spectrum of absorptance ($\alpha = 1 - T$, where T is transmittance) was converted into an absorbance spectrum for baseline detrending because the featureless baseline signal, including reflection and scattering, can be considered an additive term in absorbance. We used cubic splining at identical frequency locations for all absorbance spectra. The baseline subtracted absorbance spectrum is re-converted into an absorptance spectrum. Supplement 1 Fig. S5 shows the list of the frequency locations used for splining and two spectrum examples before and after the detrending. Due to the sample thickness, the absorptance of the $\nu(C=O)$ peak at 1730 cm^{-1} becomes larger than 0.9 at some image pixels with some polarization angles. Although the absorptance as high as 0.99 does not affect the orientation angle output theoretically [37], the nonlinearity of the detector response and the associated noise propagation can become non-negligible when $\alpha > 0.9$. Therefore, we analyze the $\delta(CH_2)$ peak at 1470 cm^{-1} to map the 3D orientation of the entire image.

3. Results

3.1. Orthogonal-pair polarization IR (OPPIR)

A scheme of the OPPIR analysis method is presented in Fig. 1 and the detailed derivation of the OPPIR analysis method can be found in Supplement 1 Note 1. Briefly, in general, the 3D orientation direction of a molecular axis can be described with the azimuthal angle (ψ), the axial angle (θ), and the rotational angle (ϕ). If the orientational distribution function of the molecular axis is cylindrically symmetric, the local orientational broadening of a molecular axis can be represented by the order parameter from the second-order Legendre polynomials ($\langle P_2 \rangle$) for polarization IR measurement. From a prior knowledge of the relative geometry of transition dipole directions in a molecule or a unit cell, we assign a vibrational mode whose transition dipole is parallel to the molecular symmetry axis as the primary mode; a vibrational mode perpendicular to the molecular symmetry as the secondary mode [37]. When the secondary modes are equally divided into two orthogonal directions, as illustrated in Fig. 1, the polarization profiles of the primary and the secondary mode absorption become out-of-phase to each other. Analytically, the polarization-dependent absorptances of the primary and the secondary modes can be expressed with an identical set of orientational variables of the molecular symmetry axis (ψ, θ, and $\langle P_2 \rangle$). For the OPPIR analysis, we assume that (1) the orientational distribution function of the primary mode represents that of the molecular axis, and (2) the order parameter

Optics EXPRESS

of the secondary mode is the same as that of the primary mode.

$$\alpha_1(\eta) = \alpha_1^{\circ}\left\{\langle P_2\rangle \sin^2\theta\cos^2(\eta-\psi) + \frac{1}{3}(1-\langle P_2\rangle)\right\} \tag{1}$$

$$\alpha_2(\eta) = \alpha_2^{\circ}\left\{\frac{\langle P_2\rangle}{2}[\sin^2\theta\sin^2(\eta-\psi) + \cos^2\theta] \;+\frac{1}{3}(1-\langle P_2\rangle)\right\} \tag{2}$$

where $\alpha_{1,2}{}^{\circ}$ is a polarization-independent parameter. From Eq. (1), ψ can be directly determined from the phase angle of $\alpha_1(\eta)$. We define polarization anisotropy as the ratio of the maximum to minimum absorptance, which can be expressed with $\langle P_2\rangle$ and $\sin^2\theta$ as

$$r_1 \equiv \frac{\alpha_{1,\max}}{\alpha_{1,\min}} = \frac{1-\langle P_2\rangle + 3\langle P_2\rangle \sin^2\theta}{1-\langle P_2\rangle} \tag{3}$$

$$r_2 \equiv \frac{\alpha_{2,\max}}{\alpha_{2,\min}} = \frac{2+\langle P_2\rangle}{2+\langle P_2\rangle - 3\langle P_2\rangle \sin^2\theta} \tag{4}$$

Then, we can determine $\langle P_2\rangle$ and $\sin^2\theta$ from the observables r_1 and r_2 by single-step, non-iterative calculation as

$$\langle P_2\rangle = \frac{r_1 r_2 - 3r_2 + 2}{r_1 r_2 - 1} \tag{5}$$

$$\sin^2\theta = \frac{r_1 r_2 - r_1 - r_2 + 1}{r_1 r_2 - 3r_2 + 2} \tag{6}$$

Supplement 1 Fig. S6 shows contours of $\langle P_2\rangle$ and $\sin^2\theta$ as a function of r_1 and r_2 using Eqs. (5) and 6. From Eq. (6), there exist two indistinguishable solutions of $\pm\theta$. This degeneracy is a fundamental limitation of this non-tomographic measurement based on purely 2D-projected polarization optical signals.

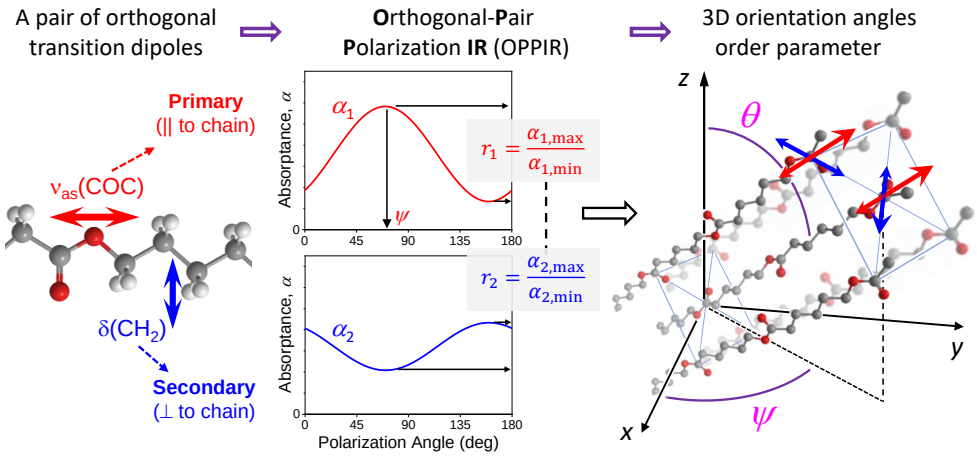

Fig. 1. A schematic presentation of the OPPIR method to determine the 3D orientation angles and the order parameter. A pair of transition dipoles are with the PCL monomer structure. The polarization anisotropy, r_1 and r_2, of the two orthogonal IR modes are used to determine $|\theta|$ and $\langle P_2\rangle$ with Eqs. (5) and (6). The phase angle of the primary mode (the black vertical arrow) is used to determine ψ. A unit cell of crystalline PCL consists of two groups of orientations. Their molecular planes (blue arrows) are oriented in two nearly orthogonal directions, while the main chains (red arrows) are parallel.

Optics EXPRESS

The OPPIR method is based on IR absorption. Compared to emission-based measurements, absorptance values are not affected by the detector sensitivity, the laser intensity, and other system-specific conditions. In addition, the absorptance values used for OPPIR are dimensionless polarization anisotropies, which is the ratio of absorptances at orthogonal polarizations. Therefore, the OPPIR calculation does not require separate measurements of the sample thickness, the molecule density, or the absolute absorption cross section, and the analysis outputs become more robust.

3.2. Polarization-controlled IR images of a PCL film

We acquired hyperspectral images of a spun-cast PCL film using a polarization-controlled IR microscope. The bright-field image of the PCL film of Fig. 2(a) shows well-defined domains, sizing from 50 µm to 100 µm. Individual spherulites are also recognizable in the polarization-controlled IR images in Figs. 2(b),(c). In the polarized IR images constructed by the ν_{as}(COC) at 1244 cm^{-1}, bow-tie patterns appear around the nucleation center. The direction of the bow-tie pattern is perpendicular to the polarization direction of the incident light, indicating that the projection of the transition dipole of the ν_{as}(COC) mode is perpendicular to the radial direction of a spherulite.

The polarization dependence of IR modes can also be found in the polarization-controlled IR spectra in Fig. 2(d). The absorptance spectrum is baseline-subtracted by spline-detrending at each image pixel (for details of detrending parameters, see Supplement 1 Fig. S5). Among those absorption peaks in the detrended spectra, the C–O–C asymmetric stretching mode (ν_{as}(COC) at 1244 cm^{-1}) and the C–C stretching mode (ν(CC) at 1296 cm^{-1}) are known to be parallel to the polymer chain [30]; thus can be considered as the primary mode. The C = O stretching mode (ν(C = O) at 1730 cm^{-1}), the CH_2 bending mode (b(CH_2) at 1420 cm^{-1}), and the CH_2 scissoring mode (δ(CH_2) at 1470 cm^{-1}) are known to be perpendicular to the main chain direction [28,30,38,39], regarded as the secondary modes. The polarization profiles of four different IR modes measured at a single image pixel are shown in Figs. 2(e),(f). All polarization profiles follow a cosine function with a dc offset. The primary mode plots in Fig. 2(e) are out-of-phase to the secondary mode plots in Fig. 2(f). The out-of-phase-ness between the primary and secondary modes can be confirmed by the narrow distributions near 90° in the histograms of $\Delta\eta_{max}$ of the four IR band pairs shown in Fig. 2(g).

The PCL unit cell, as illustrated in Fig. 1, consists of two chain geometries by equal numbers: their main chains are parallel to each other while the C = O containing molecular planes are nearly perpendicular to each other [38,40]. This nearly orthogonally bimodal geometry of the secondary modes is consistent with the observed narrow distribution of $\Delta\eta_{max} \approx 90°$ between the primary and the secondary modes (see Supplement 1 Note 1).

3.3. 3D chain orientation images

We determine the values of ψ, $|\theta|$, and $\langle P_2 \rangle$ at each image pixel using the OPPIR method and construct the image of each value, as shown in Fig. 3. First, the image of the azimuthal angle, ψ, shown in Fig. 3(a), is constructed by the phase angle of the primary mode. The ψ image shows that polymer chain projections to the polarization plane are symmetrically aligned tangential to circumferences from the nucleation center of each spherulite. The tangential alignment of the projected chain orientation can be seen more clearly in the enlarged ψ image of Fig. 3(g). Because of the circular symmetry of the projected chain orientation in each spherulite, the distribution of ψ over the >50 spherulites becomes isotropic, as shown in the histogram of Fig. 3(b). This result of the tangential alignment of the azimuthal angles is similar to the earlier report on 2D-projected polarization IR images of non-banded PCL spherulites [18]. Although from the ψ image, we can reconfirm that PCL chains are aligned perpendicular to the radial direction, we cannot still determine the out-of-plane angle of the chains only with the ψ image.

Optics EXPRESS

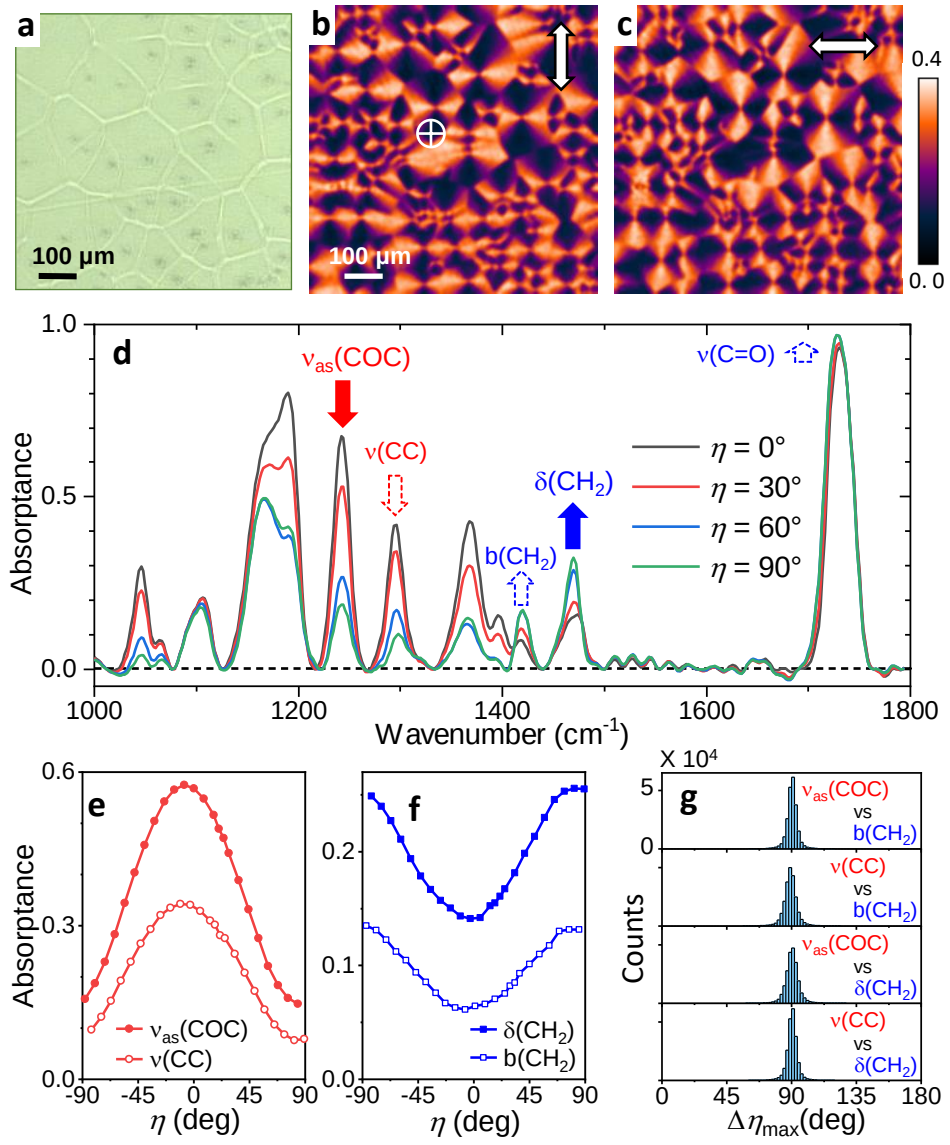

Fig. 2. Polarization-controlled infrared (IR) images and spectra of a PCL film. (a) a bright-field image of the PCL film. (b) and (c) Absorptance images by vertically- and horizontally-polarized light, respectively, acquired at 1244 cm^{-1}, corresponding to the ν_{as}(COC) band. (d) Polarization-dependent absorptance spectra at the marked location in (b). The red and blue arrows indicate IR modes whose transition dipoles are oriented parallel and perpendicular, respectively, to the chain direction. The IR modes indicated by the filled arrows are used for analysis in this paper. (e) Polarization profiles of the ν_{as}(COC) band at 1244 cm^{-1} and the ν(CC) band at 1296 cm^{-1}, which are the primary modes. (f) Polarization profiles of the b(CH$_2$) band at 1420 cm^{-1} and the δ(CH$_2$) band at 1470 cm^{-1}, which are the secondary modes. (g) The histograms of $\Delta\eta_{max}$ for various pairs of the primary and the secondary modes. The full-width-half-maximum (fwhm) of the $\Delta\eta_{max}$ ($= \eta_{max,1} - \eta_{max,2}$) distributions are 7.1°, 6.7°, 5.4°, and 5.4° (from top to bottom).

Optics EXPRESS

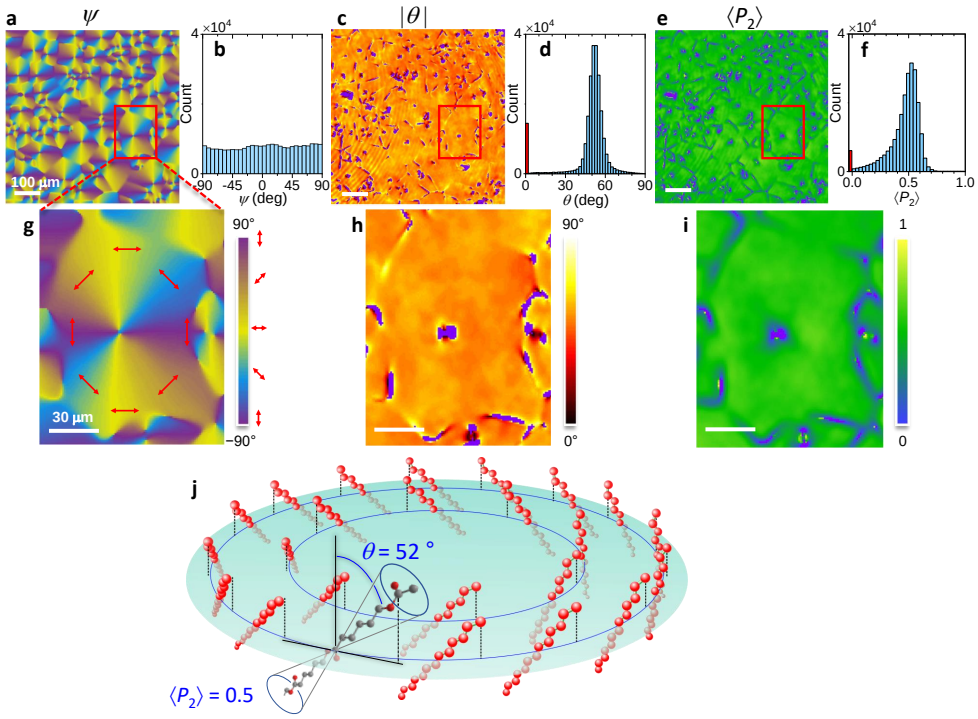

Fig. 3. Results of the 3D orientation imaging of the PCL film by OPPIR microscopy. (a) and (b) The image and the histogram of ψ. (c) and (d) The image and the histogram of $|\theta|$. (e) and (f) The image and the histogram of $\langle P_2 \rangle$. (g)–(i) Enlarged images of ψ, $|\theta|$, and $\langle P_2 \rangle$, focused on a single spherulite. The pixels of unsolvable $|\theta|$ due to $\sin^2\theta < 0$ or $\sin^2\theta > 1$ are colored as violet in the images (c) and (h) and presented as the red bar at zero in the histogram of (d). Similarly, the pixels of unsolvable $\langle P_2 \rangle$ due to $\langle P_2 \rangle < 0$ or $\langle P_2 \rangle > 1$ are represented as violet in the images (e) and (i) and as the red bars at zero in the histogram of (f). (j) An illustration of chain orientations inside a spherulite is constructed based on the observed 3D orientation angles.

In Figs. 3(c),(h), the original-sized and enlarged images of $|\theta|$ do not exhibit any distinguishable variations per spherulite but appear nearly uniform overall except for the nucleation centers and the spherulite boundaries. The histogram of $|\theta|$ in Fig. 3(d) shows a narrow distribution centering at 52° with a full-width-half-maximum (fwhm) of 8°. Based on the observed ψ and $|\theta|$, the orientation of PCL chains in a spherulite can be illustrated as orthogonal to the crystal growth direction and tilted by 52° from the normal vector of the sample film (Fig. 3(j)). It must be noted that we do not know the helicity of the tilted chains because the sign of θ cannot be determined only by the OPPIR method.

The original-sized and enlarged $\langle P_2 \rangle$ images in Figs. 3(e),(i) look flat over the crystal growth region. Similar to $|\theta|$, $\langle P_2 \rangle$ values decrease near the nucleation centers and the boundaries of spherulites. The histogram of Fig. 3(f) shows a slightly asymmetrical distribution of $\langle P_2 \rangle$ with a long tail toward zero. The median value is 0.51, and the fwhm of 0.15. The outlier values of $|\theta|$ and $\langle P_2 \rangle$ near the nucleation centers and the spherulite boundaries may be related to the mixing of multiple oriental distribution functions at the interfaces. A detailed discussion including simulations can be found in Discussion.

Optics EXPRESS

4. Discussion

4.1. Unsolvable θ at the boundaries and nucleation centers

The $\sin^2\theta$ value often becomes either larger than one or smaller than zero near nucleation centers and boundaries, making θ unsolvable with Eq. (6). The fraction of those θ-unsolvable pixels with ($\sin^2\theta < 0$) or ($\sin^2\theta > 1$) is 6% of the total image pixels. Similarly, the fraction of pixels where ($\langle P_2 \rangle < 0$) or ($\langle P_2 \rangle > 1$) is 3% of the image in Fig. 3(e). We cannot determine the exact origin of the unsolvable θ and $\langle P_2 \rangle$ solely based on the current data set. First, we can consider scattering near discontinuous locations like nucleation centers and boundaries. If the scattering cross section is comparable to the absorption cross section, and the polarization dependence of scattering is different from that of IR absorption, the polarization profile of transmittance and absorptance can be different from that of the pure orientation-dependent absorption. Compared to typical IR bandwidth, however, scattering varies slowly with wavelength; thus, the detrending process performed to each absorptance spectrum should be able to minimize the contribution of polarization-dependent scattering, if any.

Another possible origin is the mixing of multiple orientations within the probing area near discontinuous regions, such as nucleation centers and boundaries. The algorithm of OPPIR is based on the assumption that the orientation distribution function of the main chains is uniaxially or cylindrical with respect to the local mean orientation direction (see Supplement 1 Note 1). At the nucleation centers and boundaries, the orientation distribution function can deviate from a cylindrical symmetry due to the overlapping of multiple crystal growth planes. We test this hypothesis using a simple model of an interface between two uniaxial orientational distribution functions with different in ψ but the same θ and $\langle P_2 \rangle$ (Fig. 4). Interestingly, although the two constituting orientations are identical in θ and $\langle P_2 \rangle$, the simulated $\sin^2\theta$ and $\langle P_2 \rangle$ values become smaller in the mixed region than the original $\sin^2\theta$ and $\langle P_2 \rangle$ values. The decrease in $\sin^2\theta$ and $\langle P_2 \rangle$ is observed in the experimental results of the images and the line scans. Interestingly, the decrease in $\sin^2\theta$ and $\langle P_2 \rangle$ appears significant at the boundaries where the encountering ψ are different (See the black lines in Figs. 4(l)–(n)). On the contrary, the mixing effect becomes negligible at the boundaries where ψ of the encountering orientations are similar (See the white circles in Figs. 4(l)–(n). More examples can be found in Supplement 1 Fig. S7). Also, the uncertainties of $\sin^2\theta$ and $\langle P_2 \rangle$ significantly increase at the interface where ψ of the encountering orientations are non-parallel. The tested model of mixing two uniaxial orientational distribution functions shows consistent results with experimentally results both in the decrease in θ and $\langle P_2 \rangle$ and the increase in fluctuation at the boundaries.

4.2. Uncertainties associated with the OPPIR analysis

We examine how the input absorptance values affect the errors of the OPPIR output values. Assuming the error in absorptance follows a normal distribution and the relative error is not significant, we derive the error propagation for (θ and $\langle P_2 \rangle$), which can be found in Supplement 1 Note 2. We pick three image pixels in the crystal growth region in Fig. 3 and compute the uncertainties in θ and $\langle P_2 \rangle$. When the relative errors of α_1 and α_2 are assumed to be 10%, the uncertainties in θ and $\langle P_2 \rangle$ are listed in Supplement 1 Table S1. The calculated uncertainties of θ and $\langle P_2 \rangle$ are approximately 10° and 0.1, respectively. Numerically, the uncertainties of both θ and $\langle P_2 \rangle$ values increase when the polarization anisotropies, r_1 and r_2, decrease toward one because the denominators in Eqs. (5) and 6 become close to zero. r_1 and r_2 converge to one when the mean orientation becomes close to the film normal direction ($\theta \approx 0$) or the distribution becomes isotropic ($\langle P_2 \rangle \approx 0$).

We subtract the featureless baseline from an absorbance spectrum to remove the contribution of reflection, scattering, and other non-IR artifacts that are wavelength-insensitive. There are many numerical methods to determine the detrending baseline. Depending on the detrending

Optics EXPRESS

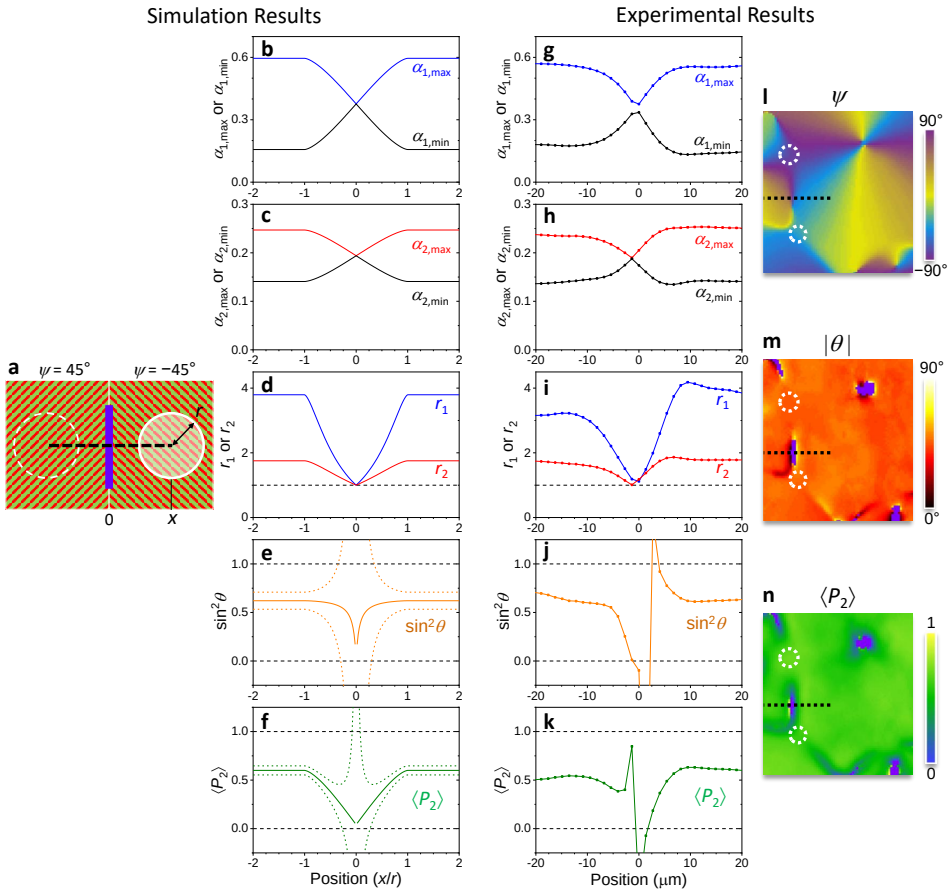

Fig. 4. The effect of the non-uniaxiality of the orientational distribution function on the OPPIR analysis. (a) We mimic the boundary between two spherulites using an interface between two uniaxial orientation distribution functions. The two orientations have the same $\theta = 45°$ and $\langle P_2 \rangle = 0.6$. However, their ψ's are different: one with $\psi = +45°$, and the other, $\psi = -45°$. The image resolution is displayed as the circle with a radius of r. (b)–(f) Simulated absorptances and the OPPIR results of the line scan from one uniaxial distribution to the mixture of two uniaxial distributions and then to the other uniaxial distribution. The orange and green dotted lines in (e) and (f) indicate the uncertainties in $\sin^2\theta$ and $\langle P_2 \rangle$, assuming 10% relative uncertainties for α_1 and α_2. (g)–(k) Line scans across a spherulite boundary of experimental results, corresponding to (b)–(f). (l)–(n) The enlarged images of Figs. 3(g)–(i). The experimental data used for (g)–(k) are copied from the dotted lines. The white dotted circles indicate boundaries where two encountering orientations are similar in ψ.

Optics EXPRESS

method, the polarization anisotropy values can vary, and the orientation output can also be affected. The dependence on the detrending condition becomes more significant when the peak height is low compared to the presumed baseline. As shown in the raw spectra and the baseline detrended spectra are shown in Supplement 1 Fig. S5, the baseline contribution is not negligible compared to the IR peak heights of interest. Based on our comparative analysis using different IR mode pairs for the primary and secondary modes, the variations of the mean θ and $\langle P_2 \rangle$ are approximately $\pm 5^\circ$ and 0.1 for different spline points, although those spline points are statistically tested. Since there are no absolute criteria to determine the proper baseline for each absorption spectrum, robust detrending will remain challenging for the measurement assurance of quantitative analysis of IR spectra.

We consider a potential effect of polarization mixing due to tight focusing. A simple numerical simulation of light (wavelength = 8 μm) focused by a lens with 0.7 NA, and the incident light is x-polarized before focusing. The light intensities of the x-, y-, and z-polarization components are averaged over a cube of (8 μm × 8 μm × 8 μm) at the focus. The ratio of the averaged intensity of the other polarization to that of the x-polarization can be considered as a metric of polarization mixing. The calculated ratios are $I_y/I_x = 0.0005$ and $I_z/I_x = 0.015$. Therefore, we do not consider polarization mixing by the 0.7 NA objective lens for the OPPIR data analysis. However, if the numerical aperture is greater, polarization mixing may need to be taken into account for more accurate measurements.

Optical imaging of thin films is often hindered by destructive interference between light reflected from different interfaces. The fringes become non-negligible when the film thickness or the gaps between the film and the substrate are similar to the light wavelength [41,42]. The interference appears as fringes in images (See Figs. 2(b),(c) and Figs. 3(c),(e)) and undulations in spectra because the interference phase changes with the light wavelength. Supplement 1 Fig. S8 shows fringe patterns in the $|\theta|$ and $\langle P_2 \rangle$ images, indicating the interference affects OPPIR results likely via spectral distortion of the IR peaks. As shown in the line scans in Supplement 1 Fig. S8, the interference can result in the variations of θ and $\langle P_2 \rangle$ of 10° and 0.1, respectively, which can be substantially challenging to OPPIR. However, it is still challenging for IR hyperspectral imaging to eliminate the spatially- and spectrally-intertwined interference without modifying experimental configurations [41,42].

5. Conclusion

We have demonstrated that a new polarization-controlled IR imaging technique based on the OPPIR can determine the 3D angles and the order parameter of the molecular orientation at each image pixel from the polarization-dependent absorption of two orthogonal IR modes. The 3D orientation maps of polymer chains in a semicrystalline PCL film were constructed from hyperspectral data measured by a high-throughput polarization-controlled wide-field QCL-IR microscope. The newly unraveled molecular information allowed us to discuss the complex hierarchical molecular structures, such as polymer spherulites and biological tissues. This versatile imaging approach is a substantial advancement from existing ensemble-based spectroscopy techniques and is, thus, capable of broadly impacting molecule-level understanding of the anisotropic structure of natural and synthetic materials.

Acknowledgments. We thank Desu Chen and Sumona Sarkar for sample preparation, Lee Richter for thickness measurements, and John Bonevich for SEM measurements. We thank Chad Snyder for discussions on polymer structures. We thank Kern Lee for drawing the background image of the thumbnail illustration. Certain commercial equipment, instruments, or materials are identified in this paper to foster understanding. Such identification does not imply endorsement by NIST, nor does it imply that the materials or equipment identified are necessarily the best available for the purpose. Official contribution of the National Institute of Standards and Technology; not subject to copyright in the United States.

Disclosures. The authors declare no conflicts of interest.

Optics EXPRESS

Data availability. Data underlying the results presented in this paper are not publicly available at this time but may be obtained from the authors upon request.

Supplemental document. See Supplement 1 for supporting content.

References

1. C. Yuan, W. Ji, R. Xing, J. Li, E. Gazit, and X. Yan, "Hierarchically oriented organization in supramolecular peptide crystals," Nat. Rev. Chem. **3**(10), 567–588 (2019).
2. J. Qiao, X. Kong, Z.-X. Hu, F. Yang, and W. Ji, "High-mobility transport anisotropy and linear dichroism in few-layer black phosphorus," Nat. Commun. **5**(1), 4475 (2014).
3. D. Liang, B. S. Hsiao, and B. Chu, "Functional electrospun nanofibrous scaffolds for biomedical applications," Adv. Drug Delivery Rev. **59**(14), 1392–1412 (2007).
4. G. L. Goh, S. Agarwala, and W. Y. Yeong, "Directed and On-Demand Alignment of Carbon Nanotube: A Review toward 3D Printing of Electronics," Adv. Mater. Interfaces **6**(4), 1801318 (2019).
5. L.-W. Jin, K. A. Claborn, M. Kurimoto, M. A. Geday, I. Maezawa, F. Sohraby, M. Estrada, W. Kaminksy, and B. Kahr, "Imaging linear birefringence and dichroism in cerebral amyloid pathologies," Proc. Natl. Acad. Sci. **100**(26), 15294–15298 (2003).
6. Y. Hikima, J. Morikawa, and T. Hashimoto, "Imaging of Two-Dimensional Distribution of Molecular Orientation in Poly(ethylene oxide) Spherulite Using IR Spectrum and Birefringence," Macromolecules **45**(20), 8356–8362 (2012).
7. W.-S. Chang, J. W. Ha, L. S. Slaughter, and S. Link, "Plasmonic nanorod absorbers as orientation sensors," Proc. Natl. Acad. Sci. **107**(7), 2781–2786 (2010).
8. V. V. Prokhorov, S. I. Pozin, O. M. Perelygina, and E. I. Mal'Tsev, "Crystallography and Molecular Arrangement of Polymorphic Monolayer J-Aggregates of a Cyanine Dye: Multiangle Polarized Light Fluorescence Optical Microscopy Study," Langmuir **34**(16), 4803–4810 (2018).
9. S. V. Plotnikov, A. C. Millard, P. J. Campagnola, and W. A. Mohler, "Characterization of the myosin-based source for second-harmonic generation from muscle sarcomeres," Biophys. J. **90**(2), 693–703 (2006).
10. N. Mazumder, G. Deka, W. W. Wu, A. Gogoi, G. Y. Zhuo, and F. J. Kao, "Polarization resolved second harmonic microscopy," Methods **128**, 105–118 (2017).
11. Y. J. Lee, C. R. Snyder, A. M. Forster, M. T. Cicerone, and W. L. Wu, "Imaging the Molecular Structure of Polyethylene Blends with Broadband Coherent Raman Microscopy," ACS Macro Lett. **1**(11), 1347–1351 (2012).
12. C. Cleff, A. Gasecka, P. Ferrand, H. Rigneault, S. Brasselet, and J. Duboisset, "Direct imaging of molecular symmetry by coherent anti-stokes Raman scattering," Nat. Commun. **7**(1), 11562 (2016).
13. A. P. Kennedy, J. Sutcliffe, and J.-X. Cheng, "Molecular Composition and Orientation in Myelin Figures Characterized by Coherent Anti-Stokes Raman Scattering Microscopy," Langmuir **21**(14), 6478–6486 (2005).
14. A. Masic, L. Bertinetti, R. Schuetz, L. Galvis, N. Timofeeva, J. W. C. Dunlop, J. Seto, M. A. Hartmann, and P. Fratzl, "Observations of multiscale, stress-induced changes of collagen orientation in tendon by polarized Raman spectroscopy," Biomacromolecules **12**(11), 3989–3996 (2011).
15. P. Koziol, D. Liberda, W. M. Kwiatek, and T. P. Wrobel, "Macromolecular Orientation in Biological Tissues Using a Four-Polarization Method in FT-IR Imaging," Anal. Chem. **92**(19), 13313–13318 (2020).
16. M. Ryu, A. Balčytis, X. Wang, J. Vongsvivut, Y. Hikima, J. Li, M. J. Tobin, S. Juodkazis, and J. Morikawa, "Orientational Mapping Augmented Sub-Wavelength Hyper-Spectral Imaging of Silk," Sci. Rep. **7**(1), 7419 (2017).
17. P. Mukherjee, A. Ghosh, N. Spegazzini, M. J. Lamborn, M. M. Monwar, P. J. DesLauriers, and R. Bhargava, "Relating Post-yield Mechanical Behavior in Polyethylenes to Spatially Varying Molecular Deformation Using Infrared Spectroscopic Imaging: Homopolymers," Macromolecules **51**(10), 3836–3844 (2018).
18. W. Kossack and F. Kremer, "Banded spherulites and twisting lamellae in poly–ε–caprolactone," Colloid Polym. Sci. **297**(5), 771–779 (2019).
19. Y. Hikima, J. Morikawa, and T. Hashimoto, "Wavenumber dependence of FT-IR image of molecular orientation in banded spherulites of poly(3-hydroxybutyrate) and poly(l-lactic acid)," Macromolecules **46**(4), 1582–1590 (2013).
20. C. Eklouh-Molinier, T. Happillon, N. Bouland, C. Fichel, M.-D. Diébold, J.-F. Angiboust, M. Manfait, S. Brassart-Pasco, and O. Piot, "Investigating the relationship between changes in collagen fiber orientation during skin aging and collagen/water interactions by polarized-FTIR microimaging," Analyst **140**(18), 6260–6268 (2015).
21. M. J. Citra, D. B. Chase, R. M. Ikeda, and K. H. Gardner, "Molecular-Orientation of High-Density Polyethylene Fibers Characterized By Polarized Raman-Spectroscopy," Macromolecules **28**(11), 4007–4012 (1995).
22. Y. Hikima, J. Morikawa, and T. Hashimoto, "FT-IR Image Processing Algorithms for In-Plane Orientation Function and Azimuth Angle of Uniaxially Drawn Polyethylene Composite Film," Macromolecules **44**(10), 3950–3957 (2011).
23. C. R. Desper and R. S. Stein, "Measurement of Pole Figures and Orientation Functions for Polyethylene Films Prepared by Unidirectional and Oriented Crystallization," J. Appl. Phys. **37**(11), 3990–4002 (1966).
24. C. P. Lafrance, M. Pézolet, and R. E. Prud'homme, "Study of the Distribution of Molecular Orientation in Highly Oriented Polyethylene by X-ray Diffraction," Macromolecules **24**(17), 4948–4956 (1991).
25. H. H. Liu, S. Schmidt, H. F. Poulsen, A. Godfrey, Z. Q. Liu, J. A. Sharon, and X. Huang, "Three-dimensional orientation mapping in the transmission electron microscope," Science **332**(6031), 833–834 (2011).
26. A. S. Eggeman, R. Krakow, and P. A. Midgley, "Scanning precession electron tomography for three-dimensional nanoscale orientation imaging and crystallographic analysis," Nat. Commun. **6**(1), 7267 (2015).

Optics EXPRESS

27. R. Brüll, R. Maria, and K. Rode, "Characterizing the three-dimensional orientation in polymers using FT-IR spectroscopy with linear polarized light," Macromol. Chem. Phys. **211**(20), 2233–2239 (2010).
28. W. Kossack, M. Schulz, T. Thurn-Albrecht, J. Reinmuth, V. Skokow, and F. Kremer, "Temperature-dependent IR-transition moment orientational analysis applied to thin supported films of poly-ε-caprolactone," Soft Matter **13**(48), 9211–9219 (2017).
29. N. Shioya, K. Tomita, T. Shimoaka, and T. Hasegawa, "Second Generation of Multiple-Angle Incidence Resolution Spectrometry," J. Phys. Chem. A **123**(32), 7177–7183 (2019).
30. T. Elzein, M. Nasser-Eddine, C. Delaite, S. Bistac, and P. Dumas, "FTIR study of polycaprolactone chain organization at interfaces," J. Colloid Interface Sci. **273**(2), 381–387 (2004).
31. A. P. Bartko and R. M. Dickson, "Imaging Three-Dimensional Single Molecule Orientations," J. Phys. Chem. B **103**(51), 11237–11241 (1999).
32. E. Toprak, J. Enderlein, S. Syed, S. A. McKinney, R. G. Petschek, T. Ha, Y. E. Goldman, and P. R. Selvin, "Defocused orientation and position imaging (DOPI) of myosin V," Proc. Natl. Acad. Sci. **103**(17), 6495–6499 (2006).
33. M. Wang, J. M. Marr, M. Davanco, J. W. Gilman, and J. A. Liddle, "Nanoscale deformation in polymers revealed by single-molecule super-resolution localization-orientation microscopy," Mater. Horiz. **6**(4), 817–825 (2019).
34. S. A. Empedocles, R. Neuhauser, and M. G. Bawendi, "Three-dimensional orientation measurements of symmetric single chromophores using polarization microscopy," Nature **399**(6732), 126–130 (1999).
35. J. N. Forkey, M. E. Quinlan, M. A. Shaw, J. E. T. Corrie, and Y. E. Goldman, "Three-dimensional structural dynamics of myosin V by single-molecule fluorescence polarization," Nature **422**(6930), 399–404 (2003).
36. Y. J. Lee, "Determination of 3D molecular orientation by concurrent polarization analysis of multiple Raman modes in broadband CARS spectroscopy," Opt. Express **23**(22), 29279–29295 (2015).
37. Y. J. Lee, "Concurrent polarization IR analysis to determine the 3D angles and the order parameter for molecular orientation imaging," Opt. Express **26**(19), 24577–24590 (2018).
38. Y. Chatani, Y. Okita, H. Tadokoro, and Y. Yamashita, "Structural Studies of Polyesters. III. Crystal Structure of Poly-ε-caprolactone," Polym. J. **1**(5), 555–562 (1970).
39. D. Lin-Vien, N. B. Colthup, W. G. Fateley, and J. G. Grasselli, "Alkanes," in *The Handbook of Infrared and Raman Characteristic Frequencies of Organic Molecules* (Academic, 1991), pp. 9–28.
40. C. Funaki, S. Yamamoto, H. Hoshina, Y. Ozaki, and H. Sato, "Three different kinds of weak C-H$\cdots$O=C inter- and intramolecular interactions in poly(ε-caprolactone) studied by using terahertz spectroscopy, infrared spectroscopy and quantum chemical calculations," Polymer **137**, 245–254 (2018).
41. A. Schönhals, N. Kröger-Lui, A. Pucci, and W. Petrich, "On the role of interference in laser-based mid-infrared widefield microspectroscopy," J. Biophotonics **11**(7), e201800015 (2018).
42. S. Ran, S. Berisha, R. Mankar, W.-C. Shih, and D. Mayerich, "Mitigating fringing in discrete frequency infrared imaging using time-delayed integration," Biomed. Opt. Express **9**(2), 832 (2018).